A Distributed Cooperative Control Based on Consensus Protocol for VSC-MTDC Systems

Weiyu Wang, Xin Yin, *Senior Member, IEEE*, Yijia Cao, *Senior Member, IEEE*, Lin Jiang, *Member, IEEE*, Yong Li, *Senior Member, IEEE*

***Abstract*--** A distributed cooperative control (DCC) strategy based on the consensus protocol is proposed for providing frequency support through voltage source converter based multi-terminal direct current transmission (VSC-MTDC) systems. The DCC consists of a local *P-V* droop controller and a cooperative agent network for cooperation control. Each agent controller is composed of a frequency regulation subagent (FRA) for frequency support and a load ratio subagent (LRA) for balancing the power sharing amongst the stations connected to the same ac grid. Moreover, to reduce the impact of the communication link failure, a topology evaluating method is proposed to select the suitable topology of the communication network via graph theory. The small signal stability analysis and the steady-state analysis are performed to investigate the stability and the consensus performance of the VSC-MTDC systems with DCC. Compared with decentralized control, the DCC can simultaneously achieve better frequency support and power sharing without leading to a large dc voltage deviation. The effectiveness of the DCC is verified by simulations on a hybrid ac/dc grid with a 7-terminal VSC-MTDC in DIgSILENT/PowerFactory under the load step change event and communication failure event.

***Index Terms*—Consensus cooperative control, communication networks, frequency regulation, VSC-MTDC.**

I. Introduction

VOLTAGE source converter-based high voltage direct current (VSC-HVDC) technology has become the prevail solutions such as back to back interface between two asynchronous power grids, integration of offshore wind farms, due to the increased capacity, and the flexible controllability such as independent active/reactive power control and bi-directionality of power flow [1]. VSC-based multi-terminal HVDC (VSC-MTDC) system with several HVDC links have been constructed for integrating multiple offshore wind farms (OWF)s, such as several successful pilot projects North-Sea offshore grid in Europe [2], and several projects in China: Nanao three-terminal, Zhoushan five-terminal, and Zhangbei four-terminal [3]. VSC-MTDC/HVDC system can provide several ancillary services to the ac grids owing to its rapid and flexible power control, such as primary frequency support, voltage support, oscillation damping [4]. The provision of primary frequency support is one of the important ancillary services through VSC-MTDC systems.

When the frequency excurses after a disturbance in ac grids, the interfaced VSC-stations can change its power output for compensating the power deficiency in ac grids and the frequency deviation can be reduced [5]. The change of dc power flow will further lead to the dc voltage variation and the power deficiency in other surrounding ac grids, which can result in frequency variation in the undisturbed ac grids [6]. The speed-governor of these ac grids then adjust the mechanical power injection for frequency regulation. Thus, the truth of frequency support by VSC-MTDC systems is to utilize the power reserves of all the connected asynchronous ac grids to compensate the power deficiency of the disturbed ac grids.

Based on the communication networks requirement, frequency support methods of the MTDC can be categorized as the following three types, i.e., global information-based centralized control[7], [8], local information based decentralized control [5], and distributed control requiring partial communication links [9], [10]. As centralized control requires communication between all units and the central controller, its performance and reliability are heavily dependent upon the status of the communication networks [11]. Without requiring communication network, decentralized control based on local information is much more prevailing than the centralized one. The local frequency information is used to regulate the dc-bus voltage and the power output of VSC-stations for frequency support, such as *P-V-f* control [5], [6], [12], and *V-I-f* control [13]. However, the decentralized control suffers from the large steady-state deviation of the dc-bus voltage due to the lack of coordination among droop coefficients of VSC-stations [8].

Based on information exchange only with their neighbors, distributed control can cooperatively achieve a common synchronization goal and has been applied in microgrids [14]–[17], as it presents better robustness and reliability to communication networks against the centralized control as only a sparse communication links required, and superior cooperative performance compared with the decentralized control [11]. Distributed control based frequency support has been proposed for the cooperative coordination between synchronous generators and VSC-stations [9], in which the controller needs to be installed in all synchronous generators.

This paper proposes a distributed cooperative control (DCC) strategy based on the consensus protocol for regulating the frequency of ac grids integrated by VSC-MTDC systems. The DCC has a two-layer hierarchical structure, as shown in Fig. 1, where the local layer is the *P-V* droop control, and the cooperative layer is a consensus protocol-based agent network

This work was supported in part by the national Natural Science Foundation of China (NSFC) under Grant 51520105011, in part by the 111 Project of China under Grant B17016, and in part by the Excellent Innovation Youth Program of Changsha of China under Grant KQ1905008.

W. Wang and Y. Cao are with the School of Electrical and Information Engineering, Changsha University of Science and Technology, Changsha 410114, China. (e-mail: WYWang@csust.edu.cn, yjcao@csust.edu.cn).

L. Jiang and X. Yin are with the Department of Electrical Engineering and Electronics, University of Liverpool, Liverpool L69 3GJ, U.K. (e-mail: ljiang@liv.ac.uk, xin.yin@liverpool.ac.uk).

Y. Li is with the College of Electrical and Information Engineering, Hunan University, Changsha 410082, China. (e-mail: yongli@hnu.edu.cn).

for cooperation. Each agent has equipped a frequency subagent (FA) and a load ratio subagent (LRA) to generate dc-bus voltage reference based on the difference of frequency/load ratio with their neighbors, which will be sent to the *P-V* droop controller for changing the power output of VSC-stations. Main contributions of this paper can be summarized as follows:

1) **Superior frequency support for ac grids and power sharing among VSC-stations**. VSC-stations can cooperatively adjust its dc-bus voltage to change the dc power flow with the frequency deviation and load ratio based on the communication with the neighbors. The DCC ensures full utilization of power reserves of ac grids and the headroom of VSC-stations for compensating the power deficiency and hence achieve a smaller frequency deviation and a balanced power-sharing between the VSC-stations fed into the same ac.
2) **Improved reliability and robustness of the communication networks**. A topology evaluating method is proposed to select the suitable topology with high reliability based on the graph theory and the "N-1" principle. The DCC with reliable communication topology has higher robustness compared with centralized control.
3) **Better steady-state performance on the dc-bus voltage**. The steady-state dc-bus voltage deviation caused by the DCC is investigated. The parameter constraints of DCC are obtained to ensure a much lower deviation of dc-bus voltage compared with the decentralized control.

The rest of the paper is organized as follows: in Section II, the system configuration and basic control scheme of the test system are introduced. The DCC and the topology selection method are investigated in Section III. In Section IV and V, the small signal stability analysis and the steady-state analysis of the test system with the DCC are investigated. Section VI presents the nonlinear simulation results. Section VI concludes the finding of this paper.

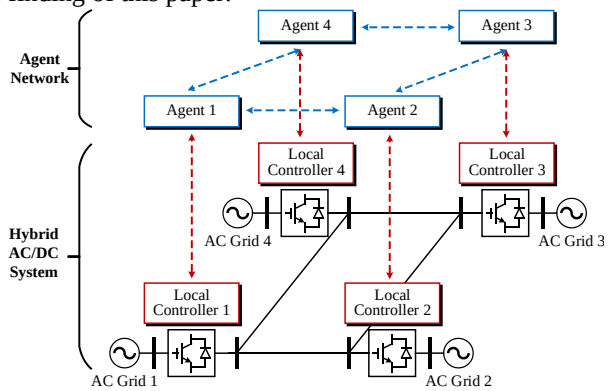

Fig. 1 Hierarchical structure of the proposed controller.

II. System Configuration and Basic Control Scheme

A. System Configuration

The general configuration of a VSC-MTDC system connecting with three asynchronous ac grids is shown in Fig. 2. For reliable power transmission, each ac grids are interfaced with several VSC-stations in case of the outage of VSC-station. The VSC 1~5 operate in the inverter mode and VSC 6 and 7 operate in the rectifier mode. Each VSC-station has a local controller and an agent controller, as shown in Fig. 1. The local controller only requires the local measurements to controller converters. The proposed primary frequency controller and load ratio controller are embedded in the agents, which can communicate with the neighbors.

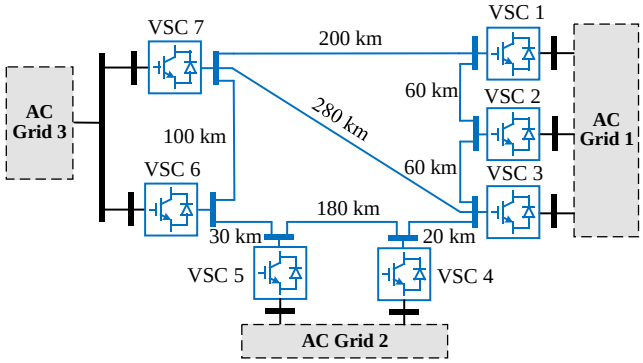

Fig. 2 Single-line diagram of the study system.

B. VSC-stations with Local P-V Controller

The local controller only focusses on the dc voltage stability of dc networks and the power sharing between VSC-stations. The hierarchical local controller is shown in Fig. 3, which is composed of classical *P-V* droop controller, power and current controller. The classical *P-V* droop control adjusts the active power output P_v of *i*-th VSC-stations according to the deviation of dc-bus voltage, which can be described as

$$P_{v,i}^{*} = P_{v0,i}^{*} + K_{v,i}(V_i - V_i^{*}) \tag{1}$$

where P_v^* and P_{v0}^* are the reference and initial reference of the active power output of VSC-stations, respectively; V and V^* represent the measurement and reference of dc-bus voltage, respectively; K_v represents the voltage droop coefficient.

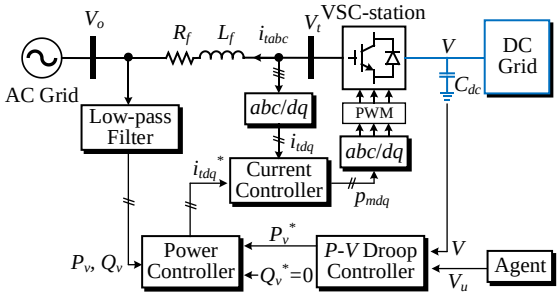

Fig. 3 The local controller of a VSC-station.

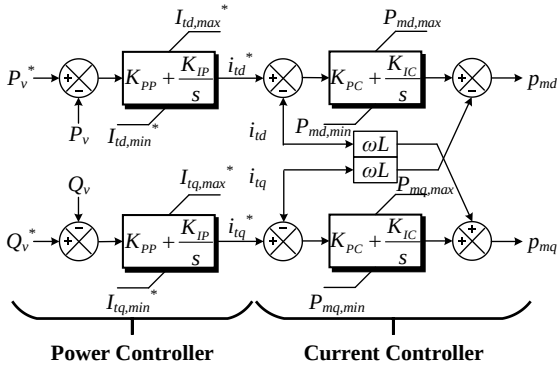

Fig. 4 Block diagram of power and current controller.

The power and current controller shown in Fig. 4 receives the power reference P_v^* from the *P-V* droop controller and generate the modulation signals for converters. According to the *P-V* droop characteristic, the power sharing between VSC-stations is dominated by the ratio of droop coefficient K_{v1}: K_{v2}:…: K_{vi} [18]. However, the local controller has no ability to respond to the frequency excursion of ac grids.

III. Consensus Protocol-based Cooperative Control

To fully utilize the power reserves in different asynchronous ac grids, the consensus protocol is employed to design the agent controller for frequency support and load ratio regulation.

A. Brief Introduction of Graph Theory

The agent network of VSC-MTDC systems can be described as a bidirectional (undirected) graph $\mathbf{G} = (\mathbf{V}, \mathbf{E})$, where $\mathbf{V} = \{v_1, v_2, \ldots, v_n\}$ is the vertex set which represents the VSC-stations and $\mathbf{E}$ is the edge set which represents the communication links. The elements of $\mathbf{E}$ can be described as (v_i, v_j). For bidirectional (undirected) graph, (v_i, v_j) is equivalent to (v_j, v_i), which means that vertex v_i and v_j can exchange data with each other. $\mathbf{N}_i$ represents the set of all the neighbors of vertex v_i, which is defined as $\mathbf{N}_i = \{j \mid (v_j, v_i) \in \mathbf{E}(\mathbf{G})\}$. The topology of agent networks can be described by the adjacency matrix $\mathbf{A} = [a_{ij}]$, where $a_{ij} = 1$ if $(v_i, v_j) \in \mathbf{E}(\mathbf{G})$ and $a_{ij} = 0$ otherwise.

B. Proposed D Cooperative Control

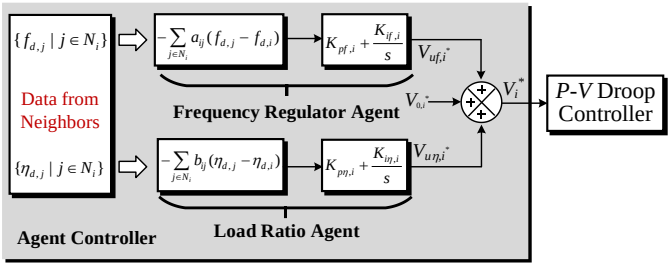

Fig. 5 Block diagram of the agent controller.

According to the droop controller (1), varying the dc voltage reference can change the power set-point of VSC-stations. An additional input signal V_u^* is added to modify the dc voltage reference and (1) is written as

$$P_{v,i}^* = P_{v0,i}^* + K_{v,i}[V_i - (V_{0,i}^* + V_{u,i}^*)] \tag{2}$$

where V_0^* represents the initial reference of dc-bus voltage.

The aim of DCC is to generate the appropriate $V_{u,i}^*$ to change the power output of VSC-stations for providing the frequency support for ac grids and balancing the power sharing between VSC-stations. The classical consensus protocol is written as [19]

$$u_i = \sum_{j \in N_i} a_{ij}(x_j - x_i) \tag{3}$$

where u_i is the input signal.

As shown in Fig. 5, two agent controllers are designed based on the consensus protocol. The frequency agent (FA) controller aims at providing the frequency support and the load-ratio agent (LRA) controller aims at regulating the load ratio of the VSC-stations integrated into the same ac grids. The sum of the output signals of FA and LRA, i.e., V_{uf} and $V_{u\eta}$, is used as the input signal u_i, which is given by

$$u_i = V_{u,i}^* = V_{uf,i}^* + V_{u\eta,i}^* \tag{4}$$

1) Frequency Subagent

FAs generate V_{uf} according to the difference of frequency deviation with their neighbors. Once the frequency deviation exceeds the threshold, FAs will calculate the frequency difference with their neighbors. The consensus protocol of FAs can be expressed as

$$\varepsilon_{f,i} = \sum_{j \in N_i} a_{ij}(f_{d,j} - f_{d,i}) \tag{5}$$

where $f_{d,i}$, $f_{d,j}$, and $\varepsilon_{f,i}$ denote the excessive frequency deviation over the threshold and their difference, respectively. $f_{d,i}$ is defined as

$$f_{d,i} = \begin{cases} (f_i - f_{0,i}) + f_{thr}, & \text{if } (f_i - f_{0,i}) < -f_{thr} \\ 0, & \text{if } |f_i - f_{0,i}| \le f_{thr} \\ (f_i - f_{0,i}) - f_{thr}, & \text{if } (f_i - f_{0,i}) > f_{thr} \end{cases} \tag{6}$$

where f_i, $f_{0,i}$ and f_{thr} represent the frequency measurements at FAs, the nominal frequency of ith ac grid and the threshold of frequency deviation, respectively. The f_{thr} can be chosen as the dead-band of the speed governor of synchronous generators.

V_{uf}^* can be obtained by the following PI controller.

$$V_{uf,i}^* = K_{Pf,i}\varepsilon_{f,i} + K_{If,i}\int \varepsilon_{f,i} dt \tag{7}$$

where K_{Pf} and K_{If} represent the proportional and integral coefficients.

2) Load Ratio Subagent

LRAs generate $V_{u\eta}^*$ according to the difference of load ratio between neighboring VSC-stations. Note that the LRAs are only applied in the VSC-stations integrated into the same ac grid. Once the VSC-stations exceed a pre-defined threshold of load ratio, LRAs will calculate the difference of load ratio with their neighbors. The consensus protocol of LRAs is obtained as

$$\varepsilon_{\eta,i} = \sum_{j \in N_i} b_{ij}(\eta_{d,j} - \eta_{d,i}) \tag{8}$$

where $\eta_{d,i}$, $\eta_{d,j}$ and $\varepsilon_{\eta,i}$ are the excessive load ratio over the threshold and their difference, respectively. $\eta_{d,i}$ is defined as

$$\eta_{d,i} = \begin{cases} 0, & \text{if } \eta_i < \eta_{thr} \\ \eta_i - \eta_{thr} & \text{if } \eta_i > \eta_{thr} \end{cases} \tag{9}$$

where η_i and η_{thr} represent the measurement and the threshold of load ratio.

$V_{u\eta}^*$ can be obtained by the following PI controller.

$$V_{u\eta,i}^* = K_{P\eta,i}\varepsilon_{\eta,i} + K_{I\eta,i}\int \varepsilon_{\eta,i} dt \tag{10}$$

where $K_{P\eta}$ and $K_{I\eta}$ represent the proportional and integral coefficients.

According to the consensus controller (4), (7) and (10), the modified *P-V* droop controller (2) will change the local dc voltage reference once FAs and LRAs are activated. The dc power flow of the VSC-MTDC system will be changed until the consensus of frequency and load ratio is achieved.

C. Topology of Communication Network

To pursue the best performance of frequency support of VSC-MTDC systems, an appropriate topology of the communication network should be chosen to ensure that all the VSC-stations can participate in frequency support and load

ratio regulation. To achieve this aim, the following conditions should be considered:

a. The communication network is bidirectional, i.e., (v_i, v_j) = (v_j, v_i).
b. The FA network at least has a spanning tree.
c. The length of communication links should be as short as possible.
d. The topology should meet the "N-1 principle", i.e., the topology still has a spanning tree under a single communication link failure.

For the candidates of topology, the **condition a-c** are easy to be checked. The **condition c** ensures the low investment of the communication network. To meet the **condition d**, the algebraic connectivity λ_2 of the candidate topology with a single communication failure should be examined. According to the graph theory, the second smallest eigenvalue λ_2 (also called the algebraic connectivity) of Laplacian matrix **L** is an important index to measure the connectivity of a graph **G**, where **L(G)** = [l_{ij}] and l_{ij} is defined as

$$l_{ij} = \begin{cases} -a_{ij}, & \text{if } i \neq j \\ \sum_{j \in N_i} a_{ij}, & \text{if } i = j \end{cases} \tag{11}$$

Assume that the probability of the loss of each edge is identical. A subgraph $\mathbf{G_s}$ of a given topology **G** can be obtained by randomly removing an edge from **G**. The Monte Carlo method is used to randomly generate a lot of subgraphs and to calculate the expected value $\bar{\lambda}_2$ of these subgraphs

$$\bar{\lambda}_2 = \frac{1}{N} \sum_{m=1}^{N} \lambda_{2,m}(\mathbf{G}_{\mathbf{s},m}) \tag{12}$$

Large $\bar{\lambda}_2$ indicates the strong connectivity of the graph under a single communication link failure.

For the test system shown in Fig. 2, six alternative topologies of the communication network shown in Fig. 6 are tested by the proposed method. The distance between the neighbors is assumed as 1. Here only is the topology of the FRA network investigated. 1000 samples are generated for each topology and the $\bar{\lambda}_2$ is calculated as shown in Table I.

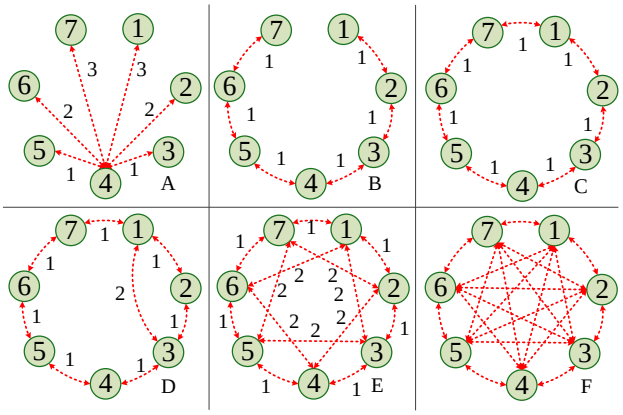

Fig. 6 Alternative topologies of the communication network.

As shown in Table I, both graphs have at least a spinning tree. The graph A suggests a centralized control type as all the VSC-stations need to communicate with a same VSC-station. The graph F has the largest $\bar{\lambda}_2$ amongst others but also leads to the huge cost of the communication network due to the longest length of the communication links. The graph D is a well-balanced topology with short length of communication links and relatively large $\bar{\lambda}_2$. Consequently, the graph D is chosen as the topology of the communication network.

TABLE I. PERFORMANCE INDEX OF TOPOLOGIES

Index \ Graph	A	B	C	**D**	E	F
Total length	12	6	7	**9**	21	42
$\bar{\lambda}_2$	0	0	0.198	**0.403**	2.304	5

D. Impact of Communication Delay

The communication network inevitably introduces communication delays, which have a significant impact on the dynamics of performance of the proposed DCC. The communication delays are determined by the communication medium, link length, bandwidth, and other factors [20]. The topology sifted out by the proposed evaluating method has a short length of each communication link, which could mitigate the communication delay to some extent. However, when the centralized control and DCC suffer from the same delays, the system dynamics with DCC could be worse. The design of a delay-dependent controller is an important task for power systems with communication networks, and there are a lot of references to investigate this topic [20]-[24]. To show the impact of the communication delays, a comparison of the system dynamics with DCC and the centralized control under the same communication delay is investigated in Section VI.E.

IV. SMALL SIGNAL STABILITY ANALYSIS

The small signal stability analysis of the closed-loop model of hybrid ac/dc power systems with the proposed DCC controller is investigated to show the effect of controller parameters on system dynamics. The state space model consists of two parts, i.e., the VSC-MTDC system and the surrounding ac grids.

A. State-Space Model of Hybrid AC/DC Power Systems

The model of VSC-stations includes the local controller and the converter model. When the inner controller is well-tuned, the dynamic model of the VSC-station and the inner controller can be simplified as Low Pass Filters (LPF) with a small time constant T_c (T_c is typically chosen in the range of 0.5-5ms) [25]. The dynamics of VSC-stations can be described as

$$\begin{cases} \dot{\phi}_i = P_{vref,i} - P_{v,i} \\ I_{dref,i} = K_{P,i}(P_{vref,i} - P_{v,i}) + K_{I,i}\phi_i \\ P_{v,i} = U_{d,i}I_{d,i} + U_{q,i}I_{q,i} \\ \dot{I}_{d,i} = \dfrac{1}{T_{c,i}}(I_{dref,i} - I_{d,i}) \\ \dot{V}_i = \dfrac{1}{C_i}\sum_{j \in N_i} \dfrac{1}{R_{ij}}(V_j - V_i) - \dfrac{P_{v,i}}{C_i V_i} \end{cases} \tag{13}$$

where K_P and K_I are the proportional and integral coefficients; ϕ is the state variable representing the state of the integral term of the power controller; U_{dq} and I_{dq} are the d- and q-axis

components of ac-terminal voltage and current; N_i is the set of neighbors of the ith VSC-station; R_{ij} is the resistance of dc cable between the ith and jth VSC-station. Assume that the phase-locked loop is fast enough to ensure that U_d is always aligned with the U_a in *abc*-frame, the $U_d = |U|$ and $U_q = 0$.

The VSC-MTDC interfaces with an ac grid through one or several VSC-stations. $S_{ac,i}$ is used to represent the set of the VSC-stations fed into the ith ac grid. For the system shown in Fig.1, $S_{\text{ac},1}$={VSC1, VSC2, VSC3}, $S_{\text{ac},2}$={VSC4, VSC5}, $S_{\text{ac},3}$={VSC6, VSC7}. Each ac grid is modeled by a single aggregated synchronous generator with a speed governor. Considering the frequency-dependent load and non-reheat turbine [26], the dynamics of the i-th ac grid is described as

$$\begin{cases} 2H_i \dot{f}_i = P_{m,i} + \sum_{j \in S_{ac,i}} P_{v,j} - P_{e,i} \\ P_{e,i} = P_{l,i} + D_i (f_i - f_{0,i}) \\ \dot{G}_i = -\dfrac{K_{f,i}}{T_{g,i}} (f_i - f_{0,i}) - \dfrac{1}{T_{g,i}} G_i \\ \dot{P}_{m,i} = \dfrac{1}{T_{CH,i}} (G_i - P_{m,i}) \end{cases} \tag{14}$$

where H denotes the inertia time constant; P_m, P_v, and P_e are the mechanical power input, the injected power from VSC-stations, and the electrical power, respectively; P_l is the non-frequency-sensitive load; f_0 and f represent the nominal measurement value of frequency, respectively; D is the load-damping constant; T_g is the time constant of governor; K_f is the speed droop coefficient; G is the valves/gate position of turbines; T_{CH} is the time constant of main inlet volumes and steam chest.

Assume a n-terminal VSC-MTDC system connects with m ac grids. The open-loop model of the whole hybrid ac/dc power systems can be obtained by linearizing (13) and (14).

$$\begin{cases} \mathbf{\Delta \dot{x}} = \mathbf{A \Delta x} + \mathbf{B \Delta u} + \mathbf{B_d \Delta d} \\ \mathbf{\Delta y} = \mathbf{C \Delta x} \end{cases} \tag{15}$$

where $\mathbf{\Delta x} = [\mathbf{\Delta x_{ac,1}}^T, \ldots, \mathbf{\Delta x_{ac,}}_m{}^T, \mathbf{\Delta x_{dc,1}}^T, \ldots, \mathbf{\Delta x_{dc,}}_n{}^T]^T$, $\mathbf{\Delta x_{ac,}}_i = [\Delta f_i \ \Delta G_i \ \Delta P_{m,i}]^T$, $\mathbf{\Delta x_{dc,}}_i = [\Delta V_i \ \Delta I_{d,i} \ \Delta \phi_i]^T$; $\mathbf{\Delta u} = [\Delta V_{uf,1}{}^*, \Delta V_{u\eta,1}{}^*, \ldots, \Delta V_{uf,n}{}^*, \Delta V_{u\eta,n}{}^*]^T$; $\mathbf{\Delta d} = [\Delta P_{l,1}, \ldots, \Delta P_{l,m}]^T$; $\mathbf{\Delta y} = [\mathbf{\Delta f}^T \ \mathbf{\Delta \eta}^T]^T$.

Two new state variables x_{uf} and $x_{u\eta}$ are used to describe the dynamics of the integrators in (7) and (10). Rewriting (7) and (10) in the matrix format yields

$$\begin{cases} \mathbf{\Delta V_{uf}^*} = \mathbf{K_{If} \Delta x_{uf}} + \mathbf{K_{Pf} L_f C_f \Delta x} \\ \mathbf{\Delta V_{u\eta}^*} = \mathbf{K_{I\eta} \Delta x_{u\eta}} + \mathbf{K_{P\eta} L_\eta C_\eta \Delta x} \end{cases} \tag{16a}$$

$$\begin{cases} \mathbf{\Delta \dot{x}_{uf}} = \mathbf{L_f C_f \Delta x} \\ \mathbf{\Delta \dot{x}_{u\eta}} = \mathbf{L_\eta C_\eta \Delta x} \end{cases} \tag{16b}$$

where $\mathbf{L_f}$ and $\mathbf{L_\eta}$ are the Laplacian matrix of the FAs and LRAs; $\mathbf{C}_\text{f}$ and $\mathbf{C_\eta}$ are the output matrixes, which could select the frequency f and load ratio η from the state vector $\mathbf{x}$, respectively. Since the dead band functions used in (6) and (9) cannot be linearized, f_{thr} and η_{thr} are set to 0 for simplification. The closed-loop state-space model is derived as

$$\underbrace{\begin{bmatrix} \mathbf{\Delta \dot{x}} \\ \mathbf{\Delta \dot{x}_{uf}} \\ \mathbf{\Delta \dot{x}_{u\eta}} \end{bmatrix}}_{\mathbf{\Delta \dot{x}_c}} = \underbrace{\begin{bmatrix} \mathbf{A'} & \mathbf{BK_{If}} & \mathbf{BK_{I\eta}} \\ \mathbf{L_f C_f} & \mathbf{0} & \mathbf{0} \\ \mathbf{L_\eta C_\eta} & \mathbf{0} & \mathbf{0} \end{bmatrix}}_{\mathbf{A_c}} \underbrace{\begin{bmatrix} \mathbf{\Delta x} \\ \mathbf{\Delta x_{uf}} \\ \mathbf{\Delta x_{u\eta}} \end{bmatrix}}_{\mathbf{\Delta x_c}} \tag{17}$$

where $\mathbf{A'} = \mathbf{A} + \mathbf{BK_{pf} L_f C_f} + \mathbf{BK_{p\eta} L_\eta C_\eta}$.

B. Small Signal Stability Analysis

The parameters of the study system are shown in Table II. The dominant eigenvalues and the state variables whose participation factors are greater than 0.1 are shown in Table III.

One can observe from Table III that the DCC participates most of the dominant eigenvalues. All these eigenvalues are effectively dampened. The eigenvalue loci of the study system with the different parameters of FRA and LRA are shown in Fig. 7.

TABLE II. PARAMETERS OF THE TEST SYSTEM

VSC-MTDC System		**AC Grids**	
Rated VSC power: $S_{vsc1\text{-}vsc5}$=300 MVA $S_{vsc6\text{-}vsc7}$=600 MVA		Rated SG power: S_{sg1} = 16800 MVA, S_{sg2} = 3600 MVA S_{sg3} = 30000 MVA	
V_{dcn}, V_{acn}	320 kV, 110 kV		
C_i	750 μF	H_1 = 4.852s, H_2 = 6.5s, H_3 = 10s	
R_{ij}	0.01 Ω/km	D	10 p.u.
K_v	20 p.u.	K_f	20 p.u.
Tc	0.01 s	T_g	0.2 s
K_P, K_I	2 p.u., 20 p.u.	T_{CH}	0.3 s
DC Power Flow			
P_{v1} = 50MW, P_{v2} = 150MW, P_{v3} = 200MW, P_{v4} = 150MW P_{v5} = 150MW, P_{v6} = -350MWP_{v7} = -352.4MW			
Consensus Controller			
k_{pf} = 5 p.u., k_{If} = 1 p.u., $k_{p\eta}$= 0.1 p.u., $k_{I\eta}$= 1 p.u.			

TABLE III. DOMINANT EIGENVALES AND STATE VARIABLES

Number	**Eigenvalue**	**Damping ratio**	**Dominant state**
λ_9	-0.031	1	$\Delta x_{uf,1}$, $\Delta x_{uf,3}$, $\Delta x_{uf,6}$, $\Delta x_{uf,7}$, $\Delta x_{u\eta,1}$, $\Delta x_{u\eta,2}$, $\Delta x_{u\eta,6}$, $\Delta x_{u\eta,7}$
λ_{10}	-0.0794	1	$\Delta x_{uf,3}$~$\Delta x_{uf,6}$, $\Delta x_{u\eta,3}$, $\Delta x_{u\eta,6}$, $\Delta x_{u\eta,7}$
$\lambda_{11\&12}$	-1.404 ± 1.554i	0.670	Δf_3, ΔG_3, $\Delta P_{m,3}$
$\lambda_{13\&14}$	-1.461 ± 2.604i	0.489	Δf_1, ΔG_1, $\Delta P_{m,1}$
$\lambda_{15\&16}$	-1.868 ± 2.524i	0.595	Δf_2, ΔG_2, $\Delta P_{m,2}$
λ_{17}	-6.128	1	Δf_3, ΔG_3, $\Delta P_{m,3}$
$\lambda_{18\&19}$	-6.529 ± 0.76i	0.993	Δf_2, ΔG_2, $\Delta P_{m,2}$, $\Delta \phi_4$ ~ $\Delta \phi_7$
$\lambda_{20\&21}$	-6.826 ± 0.389i	0.998	Δf_1, ΔG_1, $\Delta P_{m,1}$, $\Delta \phi_1$ ~ $\Delta \phi_3$, $\Delta \phi_6$, $\Delta \phi_7$
$\lambda_{22\&23}$	-9.272 ± 1.732i	0.983	$\Delta \phi_4$, $\Delta \phi_5$, $\Delta x_{u\eta,4}$, $\Delta x_{u\eta,5}$
$\lambda_{24\&25}$	-9.498 ± 1.480i	0.988	$\Delta \phi_1$, $\Delta \phi_3$, $\Delta x_{u\eta,1}$, $\Delta x_{u\eta,3}$
$\lambda_{26\&27}$	-9.502 ± 1.482i	0.988	$\Delta \phi_1$ ~ $\Delta \phi_3$, $\Delta x_{u\eta,1}$ ~ $\Delta x_{u\eta,3}$
$\lambda_{28\&29}$	-9.613 ± 1.310i	0.991	$\Delta \phi_6$, $\Delta \phi_7$, $\Delta x_{u\eta,6}$, $\Delta x_{u\eta,7}$
λ_{30}	-9.502 ± 1.482i	1	$\Delta \phi_1$ ~ $\Delta \phi_7$

The colorbar shown in Fig. 7 indicates the damping ratio of the oscillation modes. When the parameters of FRA and LRA vary in the specified ranges, the system is generally stable, as shown in Fig. 7. As can be observed from Fig. 7(a) and (b), the FRAs have obvious effects on $\lambda_{9\text{-}16}$ and $\lambda_{18\text{-}21}$, which are related to the states of FRAs and the SGs. Increasing K_{Pf} from 5 p.u. to 55 p.u. with a step of 1 p.u. can enhance the damping ratio of the eigenvalues $\lambda_{13\text{-}16}$ but decrease that of $\lambda_{18\text{-}21}$. Fig. 7(b) indicates that the damping ratio of $\lambda_{13\text{-}16}$ is weakened by increasing K_{If} from 1 p.u. to 51 p.u. with a step of 1 p.u, and λ_9 and λ_{10} move towards the right-half plane. Fig. 7(c) and (d)

suggest that the parameters of LRAs have a significant effect on the $\lambda_{22\text{-}29}$, which are mainly related to the states of LRA and the power controllers of VSC-stations. One can observe from Fig. 7(c) that the loci of $\lambda_{22\text{-}29}$ merge at the real-axis and split into two groups of breaches by increasing $K_{P\eta}$ from 0.1 to 0.51 with a step of 0.01. One group of breach extend towards the right-half plane while the other group extends towards the left-half plane. Fig. 7(d) shows that the effect of changing $K_{I\eta}$ is similar to that of changing $K_{P\eta}$. The loci of $\lambda_{22\text{-}29}$ also divided into two groups of breaches at the real-axis by increasing $K_{I\eta}$ from 1 to 5.1 with a step of 0.1. Hence, varying the parameters of FRA and LRA has significant effects on system eigenvalues, which means that the parameters should be tuned carefully to achieve a satisfactory dynamic performance.

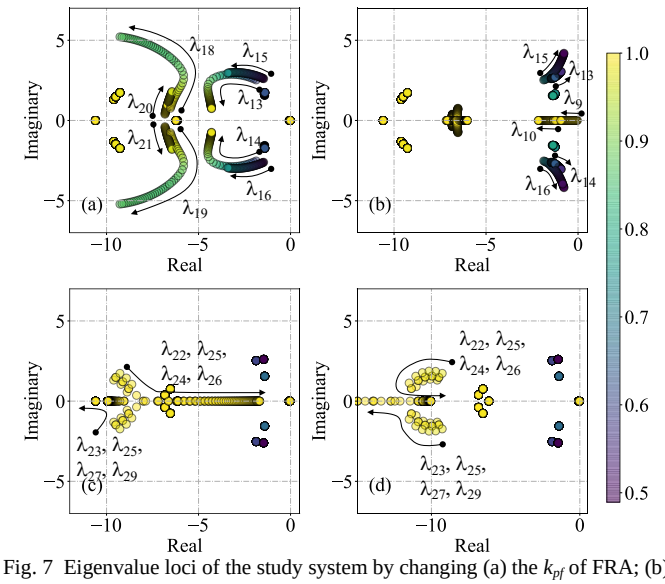

Fig. 7 Eigenvalue loci of the study system by changing (a) the k_{pf} of FRA; (b) the k_{if} of FRA; (c) the $k_{p\eta}$ of LRA; (d) the $k_{i\eta}$ of LRA.

Since the ac grids are represented by aggregated SGs, the internal oscillatory modes of ac grids cannot be observed. A hybrid ac/dc power system with detailed models will be investigated in Section VI.

C. Impact of Limiters on Control Performance

Small signal stability analysis ignores the influence of nonlinear components of VSC-stations, such as the current limiters. In some special cases, these limiters could influence the system dynamics under both small and large disturbances.

When the load change event occurs and the VSC-stations are heavily loaded, the increment of power output reference for frequency support may lead to the power or current saturation of the converters and the tracking errors of controllers. Since the power references of all the VSC-stations are determined by the cooperation of each other, the power tracking errors will break the power balance of the dc network, which could further deteriorate the dynamic dc-bus voltage and the frequency support. When short circuit faults occur, the VSC-stations may suffer from a serious impact on dc voltage and fault current. Owing to the frequency excursion during the fault period, the proposed DCC could actively reduce the power reference to restrain the frequency deviation. Hence, the impact of the fault current on converters could be attenuated. More details about the dynamic performance of DCC under both the small and large disturbances will be investigated in Section VI.D.

V. Steady-State Analysis

A. Steady-state analysis of DCC

Consider a VSC-MTDC system with n VSC-stations and m ac grids. Multiple VSC-stations may connect to the same ac grid, as shown in Fig. 8. $P_{v,j}$ represents the power output of jth VSC-station; $S_{ac,i}$ is the set of VSC-stations integrated into the ith ac grid; k_i is the number of VSC-stations in $S_{ac,i}$; $P_{dc,i}$ is the sum of the power injection from the VSC-MTDC system into the ith ac grid; $P_{m,i}$ and $P_{e,i}$ are the total power generation and the total power demand of the ith ac grid.

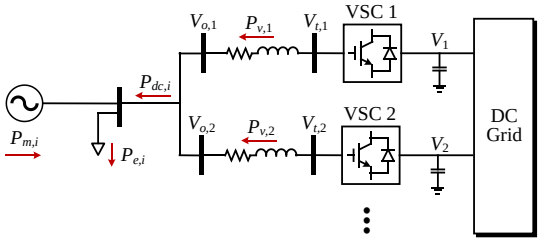

Fig. 8 Single-line diagram of an ac grid with multiple VSC-stations.

1) Steady-state frequency analysis

The derivate of the state variable x_{uf} is equal to zero at the steady-state. The Laplacian matrix $\mathbf{L_f}$ has only one zero eigenvalue with a corresponding right eigenvector $c_f\mathbf{1}_n$ [19], where c_f is a constant. Setting $\dot{\mathbf{x}}_{\mathbf{uf}} = 0$ in (16b) yields

$$\dot{\mathbf{x}}_{\mathbf{uf}} = \mathbf{L_f}\mathbf{f_d} = 0 \Leftrightarrow \mathbf{f_d^{ss}} = c_f\mathbf{1}_n \tag{18}$$

where the superscript "ss" represents the steady-state value.

Eq. (18) indicates that all the entries of $\mathbf{f_d}$ will converge to a common value, i.e., $f_{d,i}^{ss} = c_f$, $\forall i = 1,\ldots,m$. Note that $f_{d,i}^{ss}$ is the excessive frequency deviation over the threshold $f_{thr,i}$. The real steady-state frequency deviation Δf^{ss} is

$$\Delta f_i^{ss} = f_{d,i}^{ss} + \mathrm{sgn}(c_f) f_{thr,i} = c_f + \mathrm{sgn}(c_f) f_{thr,i} \tag{19}$$

where sgn(.) is the sign function.

To calculate the steady-state frequency deviation Δf_i^{ss} of the ith ac grid, the transfer function from the load change to the frequency deviation of ac grids should be derived. Consider a step load change ΔP_l, applying Laplace transformation to (14) yields

$$\Delta f_i(s) = \frac{-\frac{1}{s}\Delta P_{l,i} + \sum_{j\in S_{ac,j}} \Delta P_{v,j}(s)}{2H_i s(1+sT_{g,i})(1+sT_{CH,i}) + K_{f,i} + D_i} \tag{20}$$

Applying final value theorem to (20) yields

$$\Delta f_i^{ss} = \lim_{t\to\infty} \Delta f_i(t) = \lim_{s\to 0} s\Delta f_i(s) = \frac{-\Delta P_{l,i} + \sum_{j\in S_{ac,i}} \Delta P_{v,j}^{ss}}{K_{f,i} + D_i} \tag{21}$$

$P_{dc,i}^{ss}$ is used to denote the steady-state power injected into the ith ac grid by the VSC-MTDC system, which is obtained by

$$\begin{aligned} \Delta P_{dc,i}^{ss} &= \sum_{j\in S_{ac,i}} \Delta P_{v,j}^{ss} \\ &= (K_{f,i} + D_i)[c_f + \mathrm{sgn}(c_f) f_{thr,i}] + \Delta P_{l,i} \end{aligned} \tag{22}$$

Then the sum of $\Delta P_{dc,i}^{ss}$ of all the ac grids is given by

$$\begin{aligned}\sum_{i=1}^{m}\Delta P_{dc,i}^{ss} &= c_f\sum_{i=1}^{m}(K_{f,i}+D_i)\\ &+\operatorname{sgn}(c_f)\sum_{i=1}^{m}f_{thr,i}(K_{f,i}+D_i)+\sum_{i=1}^{m}\Delta P_{l,i}\end{aligned} \tag{23}$$

Assume that no energy storage device is installed in the VSC-MTDC system and the power losses of the VSC-MTDC system can be neglected. The sum of the steady-state power input and output variation of the VSC-MTDC system is equal to zero

$$\begin{aligned}\sum_{i=1}^{m}\Delta P_{dc,i}^{ss} = 0 &= c_f\sum_{i=1}^{m}(K_{f,i}+D_i)\\ &+\operatorname{sgn}(c_f)\sum_{i=1}^{m}f_{thr,i}(K_{f,i}+D_i)+\sum_{i=1}^{m}\Delta P_{l,i}\end{aligned} \tag{24}$$

From (24), the excess frequency deviation $f_{d,i}^{ss}$ can be calculated by

$$f_{d,i}^{ss} = c_f = -\frac{\operatorname{sgn}(c_f)\sum_{i=1}^{m}[f_{thr,i}(K_{f,i}+D_i)]+\sum_{i=1}^{m}\Delta P_{l,i}}{\sum_{i=1}^{m}(K_{f,i}+D_i)} \tag{25}$$

Since the sign of the frequency deviation is always opposite to the sign of the load variation in the process of primary frequency regulation, sgn(c_f) in (25) can be replaced by $-\operatorname{sgn}(\sum_{i=1}^{m}\Delta P_{l,i})$. Then the frequency deviation Δf_i^{ss} of the ith ac grid is given by

$$\Delta f_i^{ss} = c_f - \operatorname{sgn}(\sum_{i=1}^{m}\Delta P_{l,i})\, f_{thr,i} \tag{26}$$

Subsequently, the steady-state variation of $P_{dc,i}^{ss}$ can be calculated by

$$\Delta P_{dc,i}^{ss} = (K_{f,i}+D_i)\Delta f_i^{ss} + \Delta P_{l,i} \tag{27}$$

If $f_{thr,i}$ is set to 0, the frequency deviation of all the ac grids will converge to the same value

$$\Delta f_i^{ss} = f_{d,i}^{ss} = -\frac{\sum_{i=1}^{m}\Delta P_{l,i}}{\sum_{i=1}^{m}(K_{f,i}+D_i)} \tag{28}$$

Eqs. (25) and (26) indicate that the frequency deviation of the ith ac grid is determined by the load change and the capacity of the primary frequency regulation of all the ac grids. Equation (27) indicates that once the frequency of an ac grid drops with the load increment, the VSC-MTDC system will inject more power into the disturbed ac grid to restore the frequency, and reduce the power injected into the undisturbed ac grids for the balance of dc power flow. This power reduction can result in the frequency deviation in the undisturbed ac grids, which can be further restrained by the speed-governors of SGs. Thus, all the ac grids connected to the VSC-MTDC system could share the power reserves and participate in the primary frequency regulation according to the redistribution of dc power flow.

The power reserve of an ac grid determines to what extent the ac grid can participate in the primary frequency regulation through the VSC-MTDC system. The participation degree can be adjusted by the frequency deviation threshold f_{thr}. For the ac grid with a low power reserve, a small f_{thr} in (6) is preferred to ensure its own frequency level.

Energy markets govern the power flows for economic operation. However, during the process of primary frequency regulation, it is a matter of great urgency to restrain the frequency excursion, and the power output of SGs are determined by the natural responses of the speed-governor of SGs. Considering the time-varying power reserves of ac grids, f_{thr} should be updated to match with the power reserves by the transmission system operator (TSO) at regular time intervals.

2) *Steady-state load ratio analysis*

Similar to the analysis of steady-state frequency, setting $\dot{\mathbf{x}}_{\boldsymbol{\omega\eta}} = 0$ yields

$$\dot{\mathbf{x}}_{\boldsymbol{\omega\eta}} = \mathbf{L}_{\boldsymbol{\eta}}\boldsymbol{\eta}_{\mathbf{d}} = 0 \Leftrightarrow \boldsymbol{\eta}_{\mathbf{d}}^{\mathbf{ss}} = c_\eta \mathbf{1}_{k_i} \tag{29}$$

Eq. (29) indicates that all the entries of $\Delta\boldsymbol{\eta}_{\mathbf{d}}$ will converge to a common value, i.e., $\eta_{d,j}^{ss} = c_\eta$, $\forall j = 1,\ldots,k_i$. Recall that k_i is the number of VSC-stations connected with the ith ac grid and $\eta_{d,j}^{ss}$ is the excessive load ratio over the threshold η_{thr}. To calculate the load ratio variation $\eta_{d,j}$ of the jth VSC-station, the steady-state power output should be calculated first

$$P_{v,j}^{ss} = P_{v0,j} + \Delta P_{v,j}^{ss} = S_{v,j}(\eta_{thr,j} + c_\eta) \tag{30}$$

where P_{v0} is the initial power set point of the VSC-station; $S_{v,j}$ is the rated capacity of jth VSC-station.

From (30), the total power injection of VSC-MTDC system into the ith ac grid is given by

$$\begin{aligned}P_{dc,i}^{ss} &= \sum_{j\in S_{ac,i}}(P_{v0,j}+\Delta P_{v,j}^{ss})\\ &= \sum_{j\in S_{ac,i}} S_{v,j}\eta_{thr,j} + c_\eta\sum_{j\in S_{ac,i}} S_{v,j}\end{aligned} \tag{31}$$

Thus the excessive load ratio $\eta_{d,j}$ can be calculated by

$$\begin{aligned}\eta_{d,j}^{ss} &= c_\eta\\ &= \frac{P_{dc0,i}+\Delta P_{dc,i}^{ss} - \sum_{j\in S_{ac,i}} S_{v,j}\eta_{thr,j}}{\sum_{j\in S_{ac,i}} S_{v,j}}, \forall j = 1,\ldots,k_i\end{aligned} \tag{32}$$

where $P_{dc0,i} = \sum_{j\in S_{ac,i}} P_{v0,j}$; $\Delta P_{dc,i}^{ss} = \sum_{j\in S_{ac,i}} \Delta P_{v,j}^{ss}$.

During the primary frequency regulation, unbalanced power dispatch between VSC-stations may result in the overload state of some VSC-stations, which could reduce the service life of electronic devices. Therefore, LRAs pursuit a balanced power dispatch between the VSC-stations, and the power flow constraints within the ac grids are ignored. Once the power system reaches a new steady-state operating point, the TSO could adjust the power dispatch between VSC-stations for achieving an economic operation.

3) *Steady-state dc-bus voltage*

The steady-state average dc-bus voltage deviation ΔV_{aver}^{ss} is used to evaluate the impact of DCC strategy on dc-bus voltage.

$$\Delta V_{aver}^{ss} = \frac{1}{n}\sum_{i=1}^{n}\Delta V_i^{ss} \tag{33}$$

According to (1), the power output variation of the *i*th VSC-station can be calculated by

$$\Delta P_{v,i}^{ss} = K_{v,i}(\Delta V_i^{ss} - \Delta V_{u,i}^{ss*}) \tag{34}$$

Thus, $\Delta V_{aver}{}^{ss}$ can be written as

$$\Delta V_{aver}^{ss} = \frac{1}{n}\sum_{i=1}^{n}\Delta V_i^{ss} = \frac{1}{n}\sum_{i=1}^{n}\frac{\Delta P_{v,i}^{ss}}{K_{v,i}} + \frac{1}{n}\sum_{i=1}^{n}\Delta V_{u,i}^{ss*} \tag{35}$$

Assume that the VSC-stations have the same K_v to ensure the equal *P-V* droop characteristic. From (35), the first term of the right side of (35) is equal to

$$\frac{1}{n}\sum_{i=1}^{n}\frac{\Delta P_{v,i}^{ss}}{K_{v,i}} = \frac{1}{nK_v}\sum_{i=1}^{m}\Delta P_{dc,i}^{ss} = 0 \tag{36}$$

For the second term of the right side of (35), multiplying both sides of (16a) from the left with $\mathbf{1}^T\mathbf{K_{pf}}^{-1}$ and $\mathbf{1}^T\mathbf{K_{p\eta}}^{-1}$yields

$$\begin{cases} \mathbf{1}^T\mathbf{K}_{\mathbf{Pf}}^{-1}\Delta\mathbf{V}_{\mathbf{uf}}^{*} = \mathbf{1}^T\mathbf{K}_{\mathbf{Pf}}^{-1}\mathbf{K}_{\mathbf{If}}\Delta\mathbf{x}_{\mathbf{uf}} + \mathbf{1}^T\mathbf{L}_{\mathbf{f}}\mathbf{C}_{\mathbf{f}}\Delta\mathbf{x} \\ \mathbf{1}^T\mathbf{K}_{\mathbf{P\eta}}^{-1}\Delta\mathbf{V}_{\mathbf{u\eta}}^{*} = \mathbf{1}^T\mathbf{K}_{\mathbf{P\eta}}^{-1}\mathbf{K}_{\mathbf{I\eta}}\Delta\mathbf{x}_{\mathbf{u\eta}} + \mathbf{1}^T\mathbf{L}_{\boldsymbol{\eta}}\mathbf{C}_{\boldsymbol{\eta}}\Delta\mathbf{x} \end{cases} \tag{37}$$

Note that $\mathbf{L_f}$ and $\mathbf{L_\eta}$ are the Laplacian matrices. The second terms of the right side of (37) are equal to 0.

To calculate the first terms of the right side of (37), multiplying both sides of (16b) from the left with $\mathbf{1}^T$ yields

$$\begin{cases} \mathbf{1}^T\Delta\dot{\mathbf{x}}_{\mathbf{uf}} = \mathbf{1}^T\mathbf{L}_{\mathbf{f}}\mathbf{C}_{\mathbf{f}}\Delta\mathbf{x} = 0 \\ \mathbf{1}^T\Delta\dot{\mathbf{x}}_{\mathbf{u\eta}} = \mathbf{1}^T\mathbf{L}_{\boldsymbol{\eta}}\mathbf{C}_{\boldsymbol{\eta}}\Delta\mathbf{x} = 0 \end{cases} \tag{38}$$

Integrating (38) with time yields

$$\begin{cases} \mathbf{1}^T\Delta\mathbf{x}_{\mathbf{uf}}(t) = \sum_{i=1}^{n}\Delta x_{uf,i}(t) = c_{sf} \\ \mathbf{1}^T\Delta\mathbf{x}_{\mathbf{u\eta}}(t) = \sum_{i=1}^{n}\Delta x_{u\eta,i}(t) = c_{s\eta} \end{cases} \tag{39}$$

where c_{sf} and $c_{s\eta}$ are constant numbers. At t=0s, $\Delta x_{uf,i}(0) = 0$ and $\Delta x_{u\eta,i}(0) = 0$, thus

$$\begin{cases} \mathbf{1}^T\Delta\mathbf{x}_{\mathbf{uf}}(t) = \sum_{i=1}^{n}\Delta x_{uf,i}(t) = 0 \\ \mathbf{1}^T\Delta\mathbf{x}_{\mathbf{u\eta}}(t) = \sum_{i=1}^{n}\Delta x_{u\eta,i}(t) = 0 \end{cases} \tag{40}$$

Let $K_{Pf,1}$=…=$K_{Pf,n}$, and $K_{If,1}$=…=$K_{If,n}$, $K_{P\eta,1}$=…=$K_{P\eta,n}$, and $K_{I\eta,1}$=…=$K_{I\eta,n}$, substituting (40) into (37) yields

$$\begin{cases} \frac{1}{K_{Pf}}\mathbf{1}^T\Delta\mathbf{V}_{\mathbf{uf}}^{*} = \frac{K_{If}}{K_{Pf}}\mathbf{1}^T\Delta\mathbf{x}_{\mathbf{uf}} \Rightarrow \sum_{i=1}^{n}\Delta V_{uf,i}^{*} = K_{If}\sum_{i=1}^{n}\Delta x_{uf,i} = 0 \\ \frac{1}{K_{p\eta}}\mathbf{1}^T\Delta\mathbf{V}_{\mathbf{u\eta}}^{*} = \frac{K_{I\eta}}{K_{P\eta}}\mathbf{1}^T\Delta\mathbf{x}_{\mathbf{u\eta}} \Rightarrow \sum_{i=1}^{n}\Delta V_{u\eta,i}^{*} = K_{I\eta}\sum_{i=1}^{n}\Delta x_{u\eta,i} = 0 \end{cases} \tag{41}$$

Eq. (41) indicates that the sum of $\Delta V_{uf}{}^{*}$ and $\Delta V_{u\eta}{}^{*}$ are always equal to 0. Thus, the second term of the right side of (35) is

$$\frac{1}{n}\sum_{i=1}^{n}\Delta V_{u,i}^{ss*} = \frac{1}{n}\sum_{i=1}^{n}\Delta V_{uf,i}^{ss*} + \frac{1}{n}\sum_{i=1}^{m}\Delta V_{u\eta,i}^{ss*} = 0 \tag{42}$$

Finally, substituting (36) and (42) into (35) yields

$$\Delta V_{aver}^{ss} = 0 \tag{43}$$

Eq. (43) implies that in the ideal situation the proposed DCC will not change the steady-state average dc voltage variation when providing frequency support and the load ratio regulation. Owing to the change of grid losses in real power systems, there may be a small deviation of the average dc voltage.

B. Comparison with Classical P-V-f Control

The performance of the classical *P-V-f* control on frequency support and dc-bus voltage regulation are derived for comparison. The classical *P-V-f* control can be expressed as

$$P_{v,i}^{*} = P_{v0,i}^{*} + K_{v,i}[V_i - (V_i^{*} + K_{vf,i}(f_i - f_{0,i}))] \tag{44}$$

where K_{vf} represents the frequency droop coefficient. Linearizing (44) yields

$$\Delta P_{v,i}^{*} = K_{v,i}\Delta V_i - K_{v,i}K_{vf,i}\Delta f_i \tag{45}$$

$\Delta V_{aver}{}^{ss}$ can be calculated by

$$\begin{aligned} \Delta V_{aver}^{ss} &= \frac{1}{n}\sum_{i=1}^{n}\Delta V_i^{ss} = \frac{1}{n}\sum_{i=1}^{n}\frac{\Delta P_{v,i}^{ss}}{K_{v,i}} + \frac{1}{n}\sum_{i=1}^{n}K_{vf,i}\Delta f_i^{ss} \\ &= \frac{1}{nK_v}\sum_{i=1}^{m}\Delta P_{dc,i}^{ss} + \frac{1}{n}\sum_{i=1}^{n}K_{vf,i}\Delta f_i^{ss} = \frac{1}{n}\sum_{i=1}^{n}K_{vf,i}\Delta f_i^{ss} \end{aligned} \tag{46}$$

Comparing (46) with (43), $\Delta V_{aver}{}^{ss}$ of *P-V-f* control is determined by the droop coefficient K_{vf} and the frequency deviation. Thus, *P-V-f* control often leads to a larger dc-bus voltage deviation than DCC.

VI. Case Studies

The ac grid 1 and the ac grid 2 in Fig. 2 are replaced by the New England 39-bus system and Kunder's two-area four-machine system to verify the effectiveness of DCC. The VSC-station 1-3 connect with the AC grid 1 at bus 8, 16, and 39. The VSC-station 4 and 5 connect with the ac grid 2 at bus 7 and 9, respectively. The load demands in AC grid 1 are increased by 1.0501 times and the power generation of generators G1~G4 in the AC grid 2 are decreased by 75MW, respectively. All the speed-governors of SGs are modelled by the IEEE Type 1 model, whose droop coefficients are shown in Table IV. The test system is developed in DIgSILENT/PowerFactory.

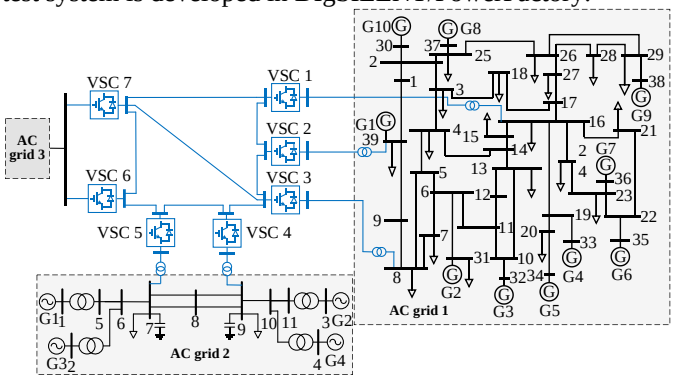

Fig. 9 The topology of the test system.

TABLE IV. Droop Coefficients of Speed-Governor

AC grid1	AC grid2	AC grid3
5 p.u.	5 p.u.	25p.u.

A. Modal Analysis and Parameter Setting

The Modal Analysis Package of DIgSILENT/PowerFactory is used to obtain the eigenvalue loci. The test system has 455 eigenvalues, and the parameters of FRA and LRA have significant effects on 28 eigenvalues, which are shown in Table V. These eigenvalues mainly related to the LRAs, SGs, Phase-Lock Loops (PLL) of VSC-stations, Power Controllers, speed-governors (GOV), automatic voltage regulators (AVR) of SGs.

TABLE V. EIGENVALES AND STATE VARIABLES

Number	Eigenvalue	Damping ratio	Related components
$\lambda_{179\&180}$	-3.756 ± 4.234i	0.664	PLL, LRA
$\lambda_{177\&178}$	-4.762 ± 4.067i	0.731	PLL, LRA, Power Controller
$\lambda_{183\&184}$	-5.59 ± 3.022i	0.88	PLL, LRA
$\lambda_{175\&176}$	-5.21 ± 3.774i	0.81	PLL, LRA
$\lambda_{199\&200}$	-2.09 ± 2.18i	0.692	PLL, LRA, SG
$\lambda_{197\&198}$	-2.913 ± 1.98i	0.827	PLL, LRA, SG
$\lambda_{185\&186}$	-0.283 ± 3.847i	0.073	SG
$\lambda_{188\&189}$	-0.052 ± 3.361i	0.016	SG
$\lambda_{257\&258}$	-0.547 ± 0.324i	0.86	GOV, SG, PLL
λ_{161}	-8.883	1	PLL, Power Controller
λ_{173}	-8.443	1	PLL, LRA, Power Controller
λ_{201}	-5.774	1	PLL, LRA, Power Controller
λ_{196}	-5.962	1	PLL, LRA, Power Controller, AVR, SG
$\lambda_{181\&182}$	-6.797 ± 1.688i	0.971	PLL, LRA, Power Controller
$\lambda_{252\&253}$	-0.375 ± 0.432i	0.656	AVR, SG
$\lambda_{232\&233}$	-0.850 ± 1.167i	0.589	AVR, SG

Most of the eigenvalues have large damping ratio while the damping ratio of $\lambda_{188\&189}$ is lower than 0.05. Although the FRAs are not deeply engaged in these eigenvalues, FRA can still influence the locations of eigenvalues, as shown in Fig. 10.

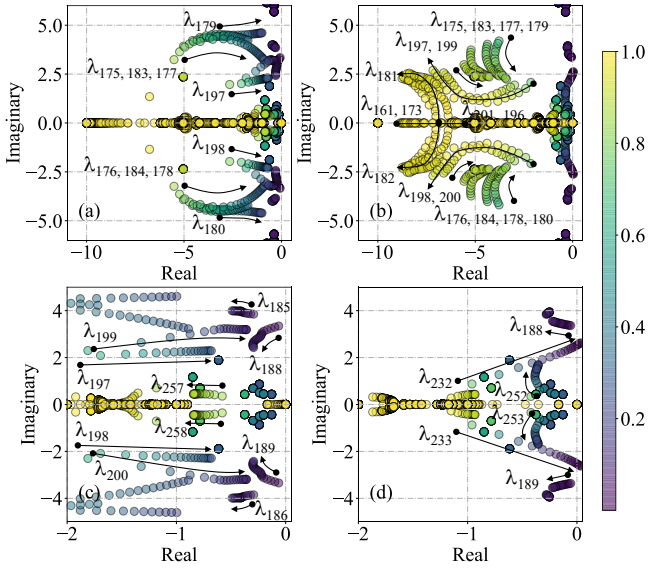

Fig. 10 Eigenvalue loci of the study system by changing (a) the k_{pf} of FRA; (b) the k_{if} of FRA. (c) Enlarged drawing of (a); (d) Enlarged drawing of (b).

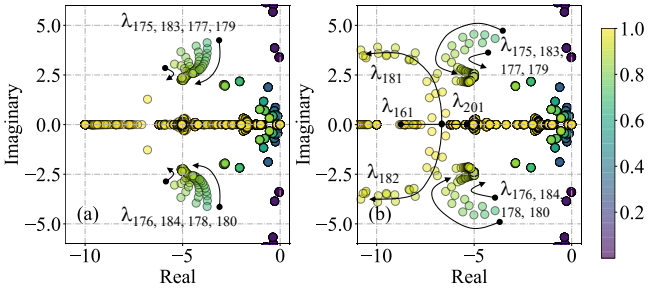

Fig. 11 Eigenvalue loci of the study system by changing (a) the $k_{p\eta}$ of LRA; (b) the $k_{i\eta}$ of LRA.

Fig. 10(a) and (b) show the loci of eigenvalues with different parameters of FRA and Fig. 10(c) and (d) are the enlarged drawing of Fig. 10(a) and (b). One can observe from Fig. 10(a) that increasing K_{Pf} can make most of the eigenvalues move towards the right-half plane, which means that the damping ratios of these eigenvalues are decreased. However, the damping ratio of some weak dampened eigenvalues, i.e., $\lambda_{185\&186}$ and $\lambda_{188\&189}$, are improved, as shown in Fig. 10(c). Increasing K_{If} can also weaken the damping of some eigenvalues, e.g., $\lambda_{232\&233}$, while that of other eigenvalues is enhanced, i.e., $\lambda_{188\&189}$, as shown in Fig. 10 (b) and (d).

Fig. 11 shows the loci of eigenvalues with different parameters of LRA. The LRA has a marginal influence on the weak dampened eigenvalues. Increasing $K_{P\eta}$ can reduce the oscillatory frequency and enhance the damping of $\lambda_{175\sim180,\ 183,\ 184}$. Increasing $K_{I\eta}$ can reduce the damping of $\lambda_{161,\ 181,\ 182,\ 201}$ but enhance that of $\lambda_{175\sim180,\ 183,\ 184}$ before they reach the inflection points. According to the comprehensive analysis of the eigenvalue loci, the parameters of FRA and LRA are selected as the ones that can enhance the damping ratio of $\lambda_{188\&189}$ and ensure that of other eigenvalues are larger than 0.05. The selected parameters are shown in Table VI.

TABLE VI. PARAMETERS OF FRA AND LRA

Parameters	VSC 1~3	VSC 4&5	VSC 6&7
f_{thr}	0.002	0.003	0.001
η_{thr}	70%		
K_{Pf}	30 p.u.		
K_{If}	15 p.u.		
$K_{P\eta}$	0.3 p.u.		
$K_{I\eta}$	0.5 p.u.		

B. Load Change Event

1) Frequency Regulation Performance

The loads in the ac grid 1 are increased by 307.901MW and the loads in the ac grid 2 are increased by 186.427MW at t=2s. The frequency deviation predicted by the steady-state analysis presented in Section V.A is compared with the time-domain simulation, as shown in Table VII. The K_{vf} of *P-V-f* control is set as 5p.u.

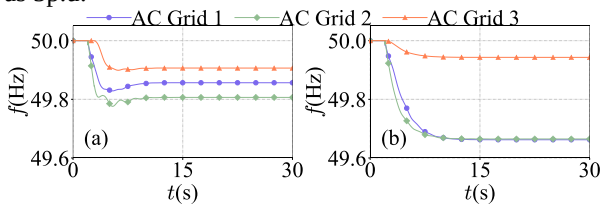

Fig. 12 The frequency of ac grids with different controllers. (a) DCC; (b) *P-V-f* control.

TABLE VII. FREQUENCY DEVIATION

Grids	Steady-state analysis	Simulations
AC grid 1	-0.0024887 p.u.	-0.0028698 p.u.
AC grid 2	-0.0034887 p.u.	-0.0038697 p.u.
AC grid 3	-0.0014887 p.u.	-0.0018696 p.u.

It can be observed that the results of the steady-state analysis are close to the time-domain simulation. Since the grid losses are ignored in the steady-state analysis, there is a small error between the predicted value and the simulations.

Fig. 12 shows the frequency variations with different control strategies. When DCC is adopted, the frequency excursions in the 39-bus system and in the two-area-four-machine system are fairly suppressed [Fig. 12 (a)] since VSC 1~5 inject more power into the adjacent ac grids for frequency support [purple curves

in Fig. 13]. The frequency nadirs of the ac grid 1 and the ac grid 2 are only 49.84Hz and 49.78Hz, respectively. The frequency of ac grid 3 is still maintained in the acceptable range (±0.2Hz). Fig. 12 (b) indicates that the frequency nadir of the ac grid 1 and the ac grid 2 with *P-V-f* control are 49.69Hz and 49.66Hz, which is much lower than that with DCC.

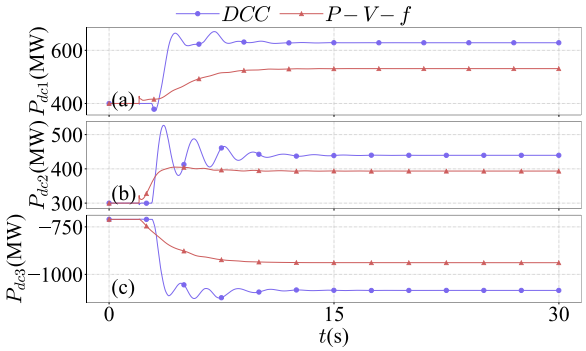

Fig. 13 The total active power injected into ac grids from VSC-MTDC: (a) AC grid 1; (b) AC grid 2; (c) AC grid 3.

2) *DC-bus Voltage Performance*

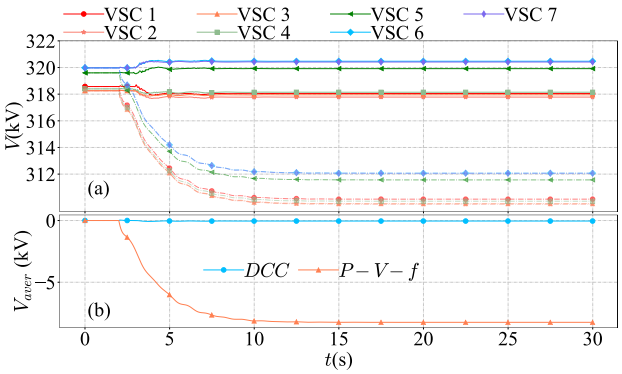

Fig. 14 The dc-bus voltage responses. (a) the dc-bus voltage; (b) the average dc-bus voltage.

Fig. 14 shows the dc-bus voltage of VSC-stations during the frequency support process. The solid lines in Fig. 14(a) represents the dc-bus voltage with the DCC and the dashed lines represent the that with the *P-V-f* droop control. Although the dc-bus voltage deviation cannot be eliminated due to the grid losses caused by the change of dc power flow, the DCC achieves a much smaller dc-bus voltage deviation compared with *P-V-f* control. As shown in Fig. 14(b), the average dc-bus voltage deviation ΔV_{aver} with DCC is nearly 0 kV. Whereas the change of ΔV_{aver} with *P-V-f* control is -8.292 kV.

3) *Load Ratio Performance*

TABLE VIII. LOAD RATIO OF VSC-STATIONS

VSC-stations	Steady-state analysis	Simulations
VSC 1~3	0.706	0.698
VSC 4&5	0.727	0.733
VSC 6&7	0.773	0.774

The load ratio of VSC-stations predicted by the steady-state analysis is compared with the time-domain simulation, as shown in Table VIII. It can be observed that the results of the steady-state analysis are close to the time-domain simulation.

The load ratio of VSC-stations is shown in Fig. 15, where only the load ratio of VSC-station 1-3 are given. When all the subagents of DCC (FRA+LRA) are activated, the power is reasonably shared by the VSC-stations fed into the same ac grid. As shown in Fig. 15(a), VSC 1 and 2 exceed the threshold η_{thre} first. Then the excess power is transmitted from VSC-station 2 and 3 to VSC 1 until both exceed η_{thre}. Finally, the equal load ratio is achieved by VSC 1~3. If only FRAs are activated, the VSC 3 has a heavy burden while VSC 1 and 2 are relatively light loaded, as shown in Fig. 15(b). When *P-V-f* control is adopted, VSC 1~3 have a proportional power increase with the frequency deviation and VSC 3 is heavy-loaded. Consequently, DCC demonstrates superior performance on frequency support, load ratio and dc-bus voltage regulation in the scenario of step load change.

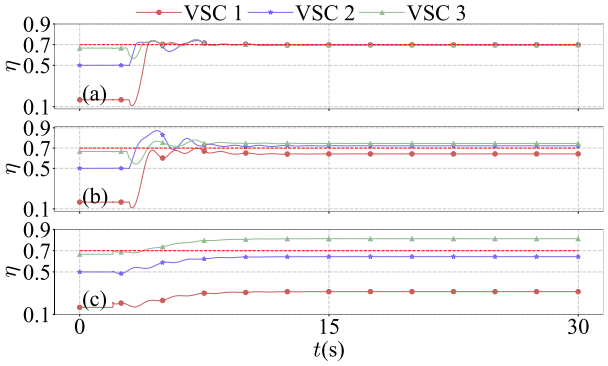

Fig. 15 The load ratio of VSC-stations during frequency support. (a) DCC (FRA+LRA); (b) only FRA; (c) *P-V-f*.

C. Influence of Power Reserves in AC Grids

If the power reserve of the ac grid 2 is not enough to participate in the frequency regulation, the thresholds of the FRAs in VSC 4 and 5 should be set to small values, e.g. $f_{thr} = 0$. To test the influence of f_{thr} on the responses of the ac grid 2, loads of the ac grid 1 are increased by 461.851 MW at t=2s. Therefore, the ac grid 2 and the ac grid 3 provide frequency support to the ac grid 1. The frequency variation and the power variation of the ac grid 2 are shown in Fig. 16 and Fig. 17.

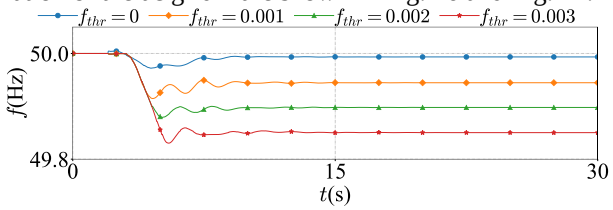

Fig. 16 The frequency of the ac grid 2 with different f_{thr}.

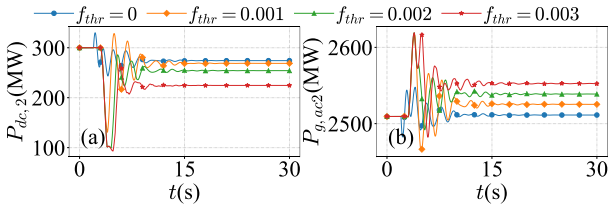

Fig. 17 The power variation of the ac grid 2 with different f_{thr}. (a) the power injection from the VSC-MTDC system; (b) the sum of the power generation of SGs in the ac grid 2.

As shown in Fig. 16 and Fig. 17, large f_{thr} can lead to large frequency deviation in the ac grid 2 because the VSC-MTDC system reduces more power transmitted to the ac grid 2. The power generation of the ac grid 2 is accordingly increased to compensate for the power deficiency, as shown in Fig. 17(b), which require large power reserves of SGs. Whilst a small f_{thr}

can lead to low frequency deviation in the ac grid 2, and the total power injection of the VSC-MTDC system and the power generation of SGs are slightly changed.

Thus, if ac grids have low power reserves, the thresholds of FRAs can be set to a small value to reduce the degree of participation in frequency support.

D. Influence of Current Limiters of VSC-Stations

1) Load Change Event

To investigate the impact of current limiters, the loads in the ac grid 1 are increased by 615.275 MW at t=2s, which is twice as much as the load increment in Section VI.B. The upper and lower current limits are set as 1.1p.u. and -1.1p.u. The system responses with and without the current limiters are shown in Figs. 18-20.

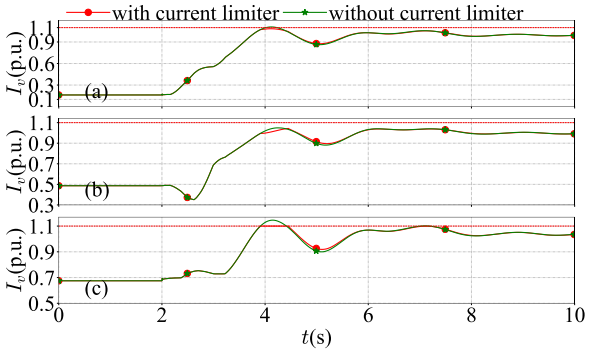

Fig. 18 The magnitude of output current of VSC-stations. (a) VSC 1; (b) VSC 2; (c) VSC 3.

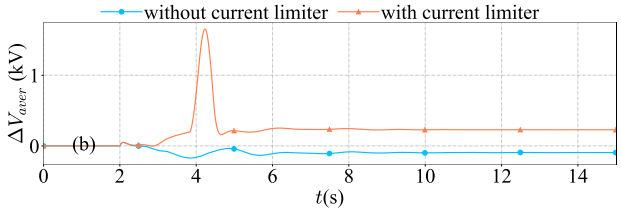

Fig. 19 The dc-bus voltage responses. (a) the dc-bus voltage; (b) the average dc-bus voltage.

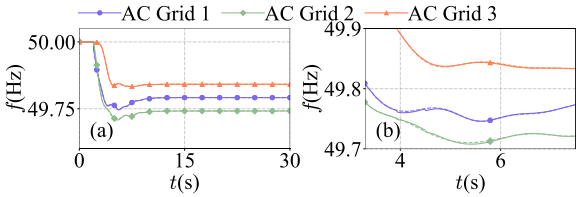

Fig. 20 The frequency of ac grids. (a) the completed plot; (b) the enlarged plot.

It can be observed from Fig. 18 that VSC 3 reach the upper current limit for about 0.5s. During this period, large dc voltage variations occur, and the average dc voltage deviation is far away from zero, as shown in Fig. 19. This is because the power output of VSC 3 cannot track the reference calculated by DCC while other VSC-stations still can, which results in the power imbalance of the dc network. The current limiters also have an impact on the frequency of ac grids, as shown in Fig. 20. However, the influence is marginal since the current limiter only reduces slight power output. When the frequency is recovered primarily by the speed-governors of synchronous generators, VSC-stations will gradually reduce the current, and the average dc voltage deviation could be approximately equal to zero again.

2) Short Circuit Fault

To investigate the system dynamics with limiters under large disturbances, a short circuit fault is applied at PCC 3 at t=2s and is cleared at t=2.12s. The system responses with and without the current limiters are shown in Figs. 21 and 22.

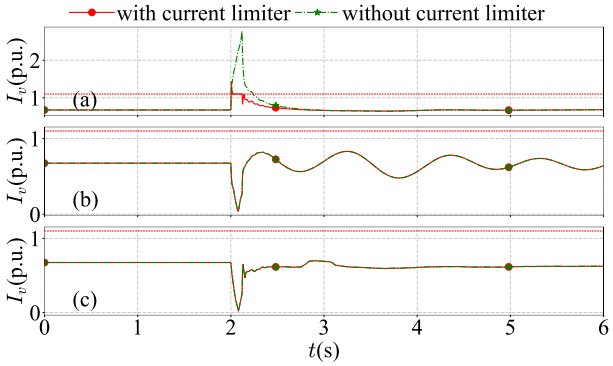

Fig. 21 The magnitude of fault current of VSC-stations. (a) under *P-V* droop control; (b) under *P-V-f* droop control; (c) under DCC.

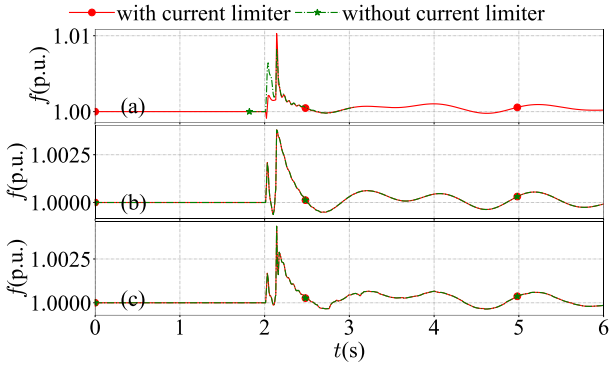

Fig. 22 The frequency of ac-terminal of VSC 3. (a) under *P-V* droop control; (b) under *P-V-f* droop control; (c) under DCC.

As shown in Fig. 21, when the proposed DCC and *P-V-f* control are adopted, the fault current of VSC 3 is reduced during the fault period. However, when the classical *P-V* control is used, the fault current of VSC 3 could exceed the upper limit. The reason is that the frequency measured at the ac-terminal of VSC 3 increase significantly during the fault period [as shown in Fig. 22], which triggers the frequency support of DCC and *P-V-f* control, and the power and current references are reduced to restrain the power injection into the disturbed ac grid. Whilst the classical *P-V* control regulates the power output only with the dc voltage deviation. The fault current would soar if there is no current limiter during the fault period, as shown in Fig. 22 (a). Hence, both the DCC and *P-V-f* control can restrain the fault current without the current limiter while the classical *P-V* control relies on the current limiter to protect the converters during the fault period.

E. Communication Disturbance

To test the dynamic performance of DCC and centralized control under the communication link failure, the step load change event used in Section VI.B occurs at t = 2s and the communication links represented by the dashed lines in Fig. 23 are cut off at t = 4s. The centralized control strategy still uses

the controllers presented in (2) ~ (10) but only the VSC 6 is selected as the central station. The other VSC-stations exchange the ac-side frequency information with the central station, which would further calculate the power output reference and send it to the VSC-stations.

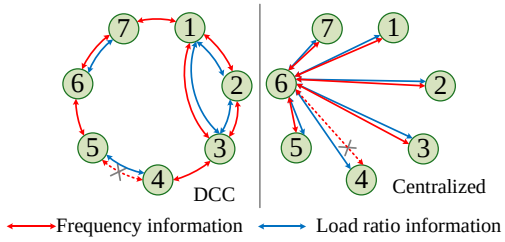

Fig. 23 The communication network of Cross and Centralized topology.

1) *Communication Link Failure*

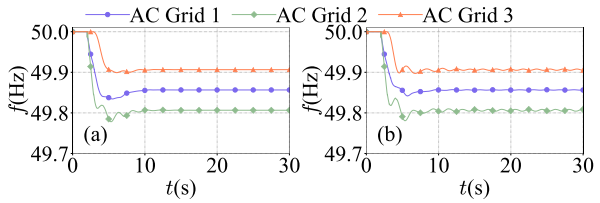

Fig. 24 The frequency variation following a communication fault. (a) DCC; (b) Centralized control.

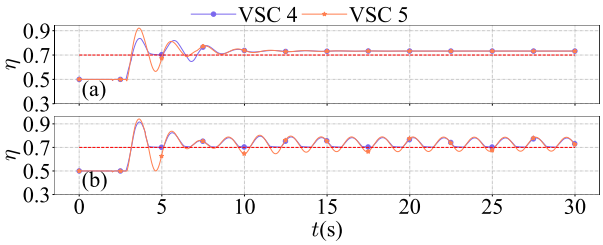

Fig. 25 The load ratio of VSC-stations during frequency support. (a) DCC; (b) Centralized control.

The dynamic responses are shown in Fig. 24 and Fig. 25. It can be observed that the communication link failure has a little impact on the system responses, as shown in Fig. 24(a) and Fig. 25(a). Whereas centralized control is more vulnerable to communication link failure. The frequency of ac grid 2 oscillates slightly over 30s, as shown in Fig. 24(b). More seriously, it can be observed from Fig. 25(b) that the load ratio of VSC-station 4 and 5 oscillate after losing the communication with the information center, which can be illustrated by the modal analysis of the system with communication failure, as shown in Table IX.

TABLE IX. EIGENVALES OF THE SYSTEM AFTER COMMUNICATION FAILURE

DCC		Centralized Control	
Eigenvalue	**Damping ratio**	**Eigenvalue**	**Damping ratio**
-0.386 ± 4.088i	0.094	-0.352 ± 6.018i	0.058
-0.526 ± 3.633i	0.143	-0.367 ± 5.685i	0.064
-0.372 ± 3.196i	0.116	-0.288 ± 3.934i	0.073
		0.036 ± 3.388i	-0.0104

According to Table IX, after communication failure, the oscillatory modes of hybrid ac/dc power system with the control of DCC has larger damping than that with centralized control. Moreover, when the centralized control is employed, a pair of unstable oscillatory modes occur after the communication failure. Thus, the hybrid ac/dc power system with DCC is more robust to the communication failure.

2) *Communication Delays*

The system dynamics with different control strategies under 500ms-delay are shown in Figs. 26 and 27. The step load change event used in Section VI.B is still employed. The communication delays are modeled by a second order Padé approximation [21], [22].

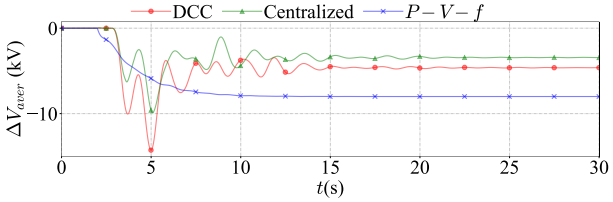

Fig. 26 The average dc-bus voltage deviation.

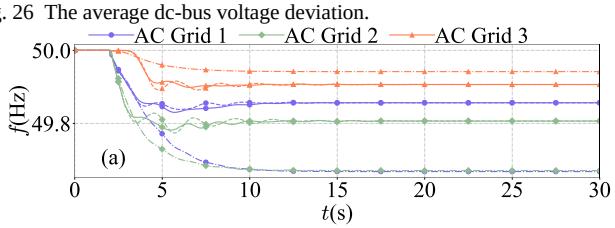

Fig. 27 The frequency of ac grids with different controllers.

It can be observed from Fig. 26 that the deviation of the average dc-bus voltage of DCC is the largest among that of other control strategies when communication delays are considered. The steady-state dc voltage deviation of DCC is also larger than that of the centralized control, but lower than that of *P-V-f* control. This phenomenon suggests that the dc-bus voltage is more susceptible to communication delays when DCC is adopted. Fig. 27 shows that both the frequency support performance of DCC and the centralized control are slightly influenced by the communication delays. Although the P-V-f control will not be affected by communication delays, its frequency deviation is the largest. Hence, under the same communication delay, the dynamic responses of dc-bus voltage could be worse while the frequency support performance is still satisfied when DCC is adopted.

However, it should be pointed out that although the centralized control has better dynamic performance under the same communication delay, the centralized control often has a larger communication delay than DCC because the central station needs to exchange information with all the other stations, which leads to heavy communication burden and packet drop [20]. Whilst the communication burden of each VSC is much less when DCC is adopted.

VII. CONCLUSIONS

This paper has investigated a distributed cooperative control strategy based on the consensus protocol for contributing the frequency support for the connected-ac grids through VSC-MTDC systems. Combining a local *P-V* droop control of each VSC-station, the DCC consists of two cooperative agents, i.e., FRA to minimize the frequency deviation and LRA to balance the power sharing among the VSC-stations fed into the same ac grid. The reliable topology of communication networks is obtained by graph theory.

The proposed DCC has been verified by simulation studies

on a hybrid ac/dc power system consists of a 7 terminal VSC-MTDC system, the two-area four-machine system, and the New England 39-bus system. Results show that the DCC can effectively utilize the power reserves in asynchronous ac grids for restoring the frequency and achieve the balanced power dispatch during the frequency support process. The cooperation amongst VSC-stations can significantly reduce the dc-bus voltage deviation caused by the frequency support and the power reallocation, compared with the decentralized control. The proposed topology evaluating method can find a suitable topology which is more robust to communication failure compared with centralized control. It should be noted that the current limiters of VSC-stations with the proposed DCC could have a negative effect on the dc voltage when some of the VSC-stations are heavily loaded. Moreover, the control performance of the proposed DCC could be deteriorated by the communication delays. In our future research, we will investigate the design of the delay-dependent distributed cooperative controller of VSC-MTDC systems.

REFERENCES

[1] N. Ray Chaudhuri, B. Chaudhuri, R. Majumder, and A. Yazdani, *Multi-terminal direct-current grids modeling, analysis, and control*. Hoboken, New Jersey: John Wiley & Sons, Ltd, 2014.

[2] T. M. Haileselassie and K. Uhlen, "Power system security in a meshed north sea HVDC grid," *Proc. IEEE*, vol. 101, no. 4, pp. 978–990, 2013.

[3] H. Pang and X. Wei, "Research on Key Technology and Equipment for Zhangbei 500kV DC Grid," *2018 Int. Power Electron. Conf. IPEC-Niigata - ECCE Asia 2018*, pp. 2343–2351, 2018.

[4] D. Van Hertem, O. Gomis-Bellmunt, and J. Liang, *HVDC GRIDS For offshore and supergrid of the Future*. Hoboken, New Jersey: John Wiley & Sons, Ltd, 2016.

[5] N. R. Chaudhuri, R. Majumder, C. Balarko, and B. Chaudhuri, "System frequency support through multi-terminal DC (MTDC) grids," *IEEE Trans. Power Syst.*, vol. 28, no. 1, pp. 347–356, 2013.

[6] B. Silva, C. L. Moreira, L. Seca, Y. Phulpin, and J. A. P. Lopes, "Provision of inertial and primary frequency control services using offshore multiterminal HVDC networks," *IEEE Trans. Sustain. Energy*, vol. 3, no. 4, pp. 800–808, 2012.

[7] Y. Wen, J. Zhan, C. Y. Chung, and W. Li, "Frequency Stability Enhancement of Integrated AC/VSC-MTDC Systems with Massive Infeed of Offshore Wind Generation," *IEEE Trans. Power Syst.*, vol. 33, no. 5, pp. 5135–5146, 2018.

[8] A. Kirakosyan, E. F. El-Saadany, M. S. El Moursi, and K. Al Hosani, "DC Voltage Regulation and Frequency Support in Pilot Voltage Droop-Controlled Multiterminal HVdc Systems," *IEEE Trans. Power Deliv.*, vol. 33, no. 3, pp. 1153–1164, 2018.

[9] M. Andreasson, R. Wiget, D. V. Dimarogonas, K. H. Johansson, and G. Andersson, "Distributed Frequency Control Through MTDC Transmission Systems," *IEEE Trans. Power Syst.*, vol. 32, no. 1, pp. 250–260, 2017.

[10] A. Musa, L. Sabug, F. Ponci, and A. Monti, "Multi-agent based intelligent frequency control in multi-terminal dc grid-based hybrid ac/dc networks," *IET Renew. Power Gener.*, vol. 12, no. 13, pp. 1434–1443, 2018.

[11] A. Bidram, V. Nasirian, A. Davoudi, and F. L. Lewis, *Cooperative synchronization in distributed microgrid control*. New York, NY, USA: Springer, 2017.

[12] O. D. Adeuyi, M. Cheah-Mane, J. Liang, and N. Jenkins, "Fast Frequency Response from Offshore Multiterminal VSC-HVDC Schemes," *IEEE Trans. Power Deliv.*, vol. 32, no. 6, pp. 2442–2452, 2017.

[13] W. Wang, Y. Li, Y. Cao, U. Hager, and C. Rehtanz, "Adaptive Droop Control of VSC-MTDC System for Frequency Support and Power Sharing," *IEEE Trans. Power Syst.*, vol. 33, no. 2, pp. 1264–1274, 2018.

[14] A. Bidram, A. Davoudi, F. L. Lewis, and J. M. Guerrero, "Distributed cooperative secondary control of microgrids using feedback linearization," *IEEE Trans. Power Syst.*, vol. 28, no. 3, pp. 3462–3470, 2013.

[15] T. Morstyn *et al.*, "Cooperative Multi-Agent Control of Heterogeneous Storage Devices Distributed in a DC Microgrid," *IEEE Trans. Power Syst.*, vol. 31, no. 4, pp. 2974–2986, 2016.

[16] A. Maknouninejad, Z. Qu, F. L. Lewis, and A. Davoudi, "Optimal, nonlinear, and distributed designs of droop controls for DC microgrids," *IEEE Trans. Smart Grid*, vol. 5, no. 5, pp. 2508–2516, 2014.

[17] D. Zhang, J. Li, and D. Hui, "Coordinated control for voltage regulation of distribution network voltage regulation by distributed energy storage systems," *Prot. Control Mod. Power Syst.*, vol. 3, no. 3, pp. 1–8, 2018.

[18] T. M. Haileselassie and K. Uhlen, "Impact of DC line voltage drops on power flow of MTDC using droop control," *IEEE Trans. Power Syst.*, vol. 27, no. 3, pp. 1441–1449, 2012.

[19] R. Olfati-Saber, J. A. Fax, and R. M. Murray, "Consensus and cooperation in networked multi-agent systems," *Proc. IEEE*, vol. 95, no. 1, pp. 215–233, 2007.

[20] B. P. Padhy, S. C. Srivastava, and N. K. Verma, "A Wide-Area Damping Controller Considering Network Input and Output Delays and Packet Drop," *IEEE Trans. Power Syst.*, vol. 32, no. 1, pp. 166–176, 2017.

[21] M. E. C. Bento, "Fixed Low-Order Wide-Area Damping Controller Considering Time Delays and Power System Operation Uncertainties," *IEEE Trans. Power Syst.*, vol. 35, no. 5, pp. 3918–3926, 2020.

[22] M. Sarkar and B. Subudhi, "Fixed low-order synchronized and non-synchronized wide-area damping controllers for inter-area oscillation in power system," *Int. J. Electr. Power Energy Syst.*, vol. 113, pp. 582–596, Dec. 2019.

[23] S. A. Hosseini, M. Toulabi, A. S. Dobakhshari, A. Ashouri-Zadeh, and A. M. Ranjbar, "Delay Compensation of Demand Response and Adaptive Disturbance Rejection Applied to Power System Frequency Control," *IEEE Trans. Power Syst.*, vol. 35, no. 3, pp. 2037–2046, 2020.

[24] L. Jiang, W. Yao, Q. H. Wu, J. Y. Wen, and S. J. Cheng, "Delay-dependent stability for load frequency control with constant and time-varying delays," *IEEE Trans. Power Syst.*, vol. 27, no. 2, pp. 932–941, 2012.

[25] A. Yazdani and R. Iravani, *Voltage-Sourced Converters in Power Systems*. 2010.

[26] P. Kundur, *Power System Stability and Control Kundur.pdf*. New York, NY, USA: McGraw-Hill,Inc., 2005.